



Kinetics of the catalytic oxidation of morin on γ -Al₂O₃ supported gold nanoparticles and determination of gold nanoparticles surface area and sizes by quantitative ligand adsorption



Matumuene Joe Ndolomingo, Reinout Meijboom*

Department of Chemistry, University of Johannesburg, PO Box 256, Auckland Park 2006, Johannesburg, South Africa

ARTICLE INFO

Article history:

Received 29 March 2016

Received in revised form 6 June 2016

Accepted 10 June 2016

Available online 13 June 2016

Keywords:

Catalytic oxidation

Morin

Kinetics

Organothiol

Chemisorption

Packing density

Surface area

Particle size

Nanoparticles

ABSTRACT

We report on the kinetic analysis of catalytic activity of γ -Al₂O₃ supported gold nanoparticles (AuNPs) on the rate of oxidation of morin by hydrogen peroxide as model reaction. Gold-based catalysts were revealed to be very active in the oxidation of morin under mild conditions, especially when Li₂O is used as additive, and cationic imidazolium ionic liquids are used as AuNPs stabilizer. All kinetic data could be modeled in terms of the Langmuir–Hinshelwood model; that is both reactants are assumed to be adsorbed on the surface of the nanoparticles. The apparent reaction rate could therefore be related to the surface of the nanoparticles, to the kinetics constant, related to the rate determining steps, and to the adsorption constant of the reactants. The organothiol adsorption-based technique for the determination of specific surface area and particle sizes of AuNPs on γ -Al₂O₃ supports is also reported. A fair agreement was found between particle sizes obtained from ligand adsorption and TEM methods. Atomic absorption spectrometry (AAS), X-ray diffraction spectrometry (XRD), N₂-physisorption (BET), transmission electron microscopy (TEM) and thermogravimetric analysis (TGA) are used for the characterization of the catalysts, while the oxidation reaction and the ligand adsorption was followed by ultraviolet-visible spectrometry (UV-vis).

© 2016 Elsevier B.V. All rights reserved.

1. Introduction

One of the features of chemical catalysis is that it regularly undergoes rapid advances. Over the past decades, catalysis of supported transition-metal nanoparticles has been striking, and received more attention for numerous reactions [1–5]. The use of transition-metal nanoparticles in catalysis is crucial as they mimic metal surface activation and catalysis at the nanoscale and thereby bring selectivity and efficiency to heterogeneous catalysis, which benefits from easy removal of catalyst materials [6]. The effective catalytic properties of the transition-metal nanoparticles are mostly based on their inherent high surface area to volume ratio [7–11]. High surface area can provide better dispersion of the active sites and easy diffusion of the reactants and, thus, makes them suitable for catalytic activity [6,10,11].

Due to their unique electromagnetic and chemical properties, gold nanoparticles (AuNPs) have been recognized as active and extraordinary effective green catalysts for various oxidation

reactions [4,12–17]. Well dispersed AuNPs on gamma-alumina (γ -Al₂O₃) support exhibit a high activity in various low-temperature oxidation reactions [4,18,19]. Gamma alumina is of catalytic interest and widely used as a support [3,4,19,20]. It has been conventionally described as a defect spinel (*Fd*-3m) with the idealized formula Al_{21+1/3□2+2/3}O₃₂, where □ denotes a vacancy [21]. Many studies have been reported on oxide-doped alumina supported AuNPs [4,19,22–25]. It was reported that lithium oxide (Li₂O) has a promoting effect on the activity of the Au/ γ -Al₂O₃ catalyst in CO oxidation [4,25]. A detailed study by Gluhov et al. [19,23,24] on the effect of the addition of alkali (earth) metals to Au/ γ -Al₂O₃ catalyst revealed that the main role of Li₂O is to stabilize the AuNPs i.e. that of a structural promoter in the investigated reactions.

As mentioned previously, the activity of heterogeneous catalysts benefits strongly from a high surface area. Yet, small nanoparticles are only kinetically stable and will aggregate to thermodynamically more stable larger particles [26], with a concomitant decrease in catalytic activity. This agglomeration is based on the principles of Ostwald ripening [26,27] as a thermodynamically driven spontaneous process because larger particles are energetically favored over smaller ones. There are numerous methods of stabilizing metal nanoparticles including the use of ionic liquids [26], polymers [28],

* Corresponding author.

E-mail address: rmeijboom@uj.ac.za (R. Meijboom).

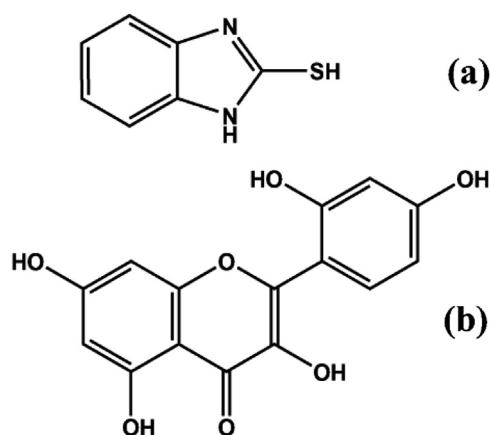


Fig. 1. Structures of (a) 2-mercaptobenzimidazole, and (b) morin dye.

low molecular weight [29] and macromolecular organic ligands [30]. Ionic liquids (ILs) have emerged as one of the most investigated classes of stabilizing agents for the synthesis and stabilization of transition-metal nanoparticles [11,26,31,32]. It may be regarded as a “nanosynthetic template” [26,33] that stabilize metal nanoparticles on the basis of their ionic nature [26,34]. The electrostatic and steric properties of ionic liquids can stabilize metal nanoparticles without the need of protective ligands [26,35–38].

Due to the nanoparticle surface roughness, size distributions, and morphological irregularity, the mechanisms involving the nanoparticle surfaces in catalytic reactions are more difficult to elucidate. As mentioned earlier, true surface area and particle size determination are key aspects of the activity of metal nanoparticle catalysts. Chemisorption methods using organothiols as probe ligands are in principle suitable for the specific surface area determination of the supported AuNPs [39–42]. It was reported that no adsorption is observed, except for CuO and AgO, when organothiols are exposed to oxidic supports [43]. Thus, it can be estimated that organothiols adsorb selectively only on AuNPs and not on γ -Al₂O₃ or Li₂O/ γ -Al₂O₃ supports. Obviously, the Au-sulfur bond is sufficiently strong to allow for binding on all gold surface atoms, even at room temperature [40].

This study aims to determine specific surface area of supported AuNPs using 2-mercaptobenzimidazole, C₇H₆N₂S (2-MBI) (Fig. 1(a)) as probe ligand, and to kinetically investigate the catalytic activities of γ -Al₂O₃ supported AuNPs on the oxidation of morin, C₁₅H₁₀O₇ under mild conditions using hydrogen peroxide, H₂O₂ in aqueous solution as model reaction.

2-MBI was chosen as the probe ligand due to its excellent solubility and stability in water, relative strong UV–vis absorbance at λ 299.7 nm, higher binding affinity with AuNPs, and small footprint for AuNPs [44]. A study by Ansar et al. showed that 2-MBI binds bidentately with AuNPs at neutral pH with a binding constant of $4.44 \pm (1.29) \times 10^6$ M⁻¹, and has a saturated packing density of 0.574 ± 0.006 nmol/cm² [45]. On the basis of this packing density, the footprint of 2-MBI on AuNPs is 0.289 nm² per molecule. It has been reported by Elzey et al. that the ligand packing density of the organothiol 3-mercaptopropionic acid (MPA) on AuNPs is size independent for AuNPs of >5 nm in diameter [46]. This suggests that ligand adsorption can be a reliable method for quantification of the AuNPs surface areas and determination of the AuNPs sizes.

Advanced oxidation processes (AOPs) have emerged as a viable method to degrade dyes in aqueous media [47,48]. The basic concept of these methods is the decomposition of H₂O₂ with the formation of free radical intermediates, especially the hydroxyl radical. This radical is capable of reacting with a variety of organic compounds leading to either partial or complete degradation. The

oxidation of morin with H₂O₂ was chosen as a model reaction to kinetically investigate the catalytic activities of γ -Al₂O₃ supported AuNPs, prior to their use in other more complex oxidation reactions. Morin (Fig. 1(b)) belongs to a group of flavonoid plant dyes [49]. These compounds are present in tea, fruits and vegetables and can be used as model compounds for studying bleaching processes in laundry detergents [50]. Its two main oxidation products are 2,4-dihydroxybenzoic acid and 2,4,6-trihydroxybenzoic acid [51,52]. The reaction mechanism of the oxidation of morin by AuNPs catalyst is not determined yet.

The catalytic degradation of morin has been carried out in the presence of manganese oxide and dendrimer-encapsulated gold nanoparticles catalysts with H₂O₂ as the oxidant [53,54]. It was demonstrated that morin dye can be decomposed using manganese oxide and dendrimer-encapsulated gold catalysts and concluded that the reaction occur on the catalyst surface. However, to the best of our knowledge, no reports are available for the use of γ -Al₂O₃ supported AuNPs as catalysts for the oxidation of morin by H₂O₂.

2. Experimental

2.1. Materials and reagents

All chemicals were at least analytical grade with high purity and were purchased from suppliers (Merck, Sigma-Aldrich and Pro-mark Chemicals). Organic dye, organothiol, peroxide, metal salts and buffer solutions were freshly prepared in 18 M Ω cm Millipore water just before the experiment.

2.2. Synthesis of catalysts

Lithium oxide on alumina was prepared via pore volume impregnation of γ -Al₂O₃ from the corresponding nitrate [3,4]. Thus, an appropriate amount of LiNO₃ was dissolved in deionized water, and the resultant salt solution was poured onto a suitable amount of γ -Al₂O₃. The prepared mixed oxide had an intended Li/Al ratio of 1/15. After calcination at 350 °C for 4 h, γ -Al₂O₃ and Li₂O/ γ -Al₂O₃ were used as supports for the gold particles. The AuNPs were prepared via homogeneous deposition precipitation using urea (CO(NH₂)₂) as precipitating agent [3,4], and afterward reduced using sodium borohydride (NaBH₄). Thus, for catalysts prepared without stabilizing agents, an appropriate amount of HAuCl₄·3H₂O was directly added to a suspension of 25 mL of deionized water containing supports, under continuous stirring. However, for catalysts with ionic liquids (ILs), the stable AuNPs were prepared in 1-butyl-3-methylimidazolium tetrafluoroborate ([BMIM][BF₄], BF₄) and 1-butyl-3-methylimidazolium hexafluorophosphate ([BMIM][PF₆], PF₆); 0.06348 mmol of BF₄ and PF₆, were added dropwise under vigorous stirring to 5 mL of aqueous solutions of HAuCl₄·3H₂O. After vigorous stirring, the mixture was then added to a suspension of de-ionized water containing supports. The intended M/Al ratio was 1/75 (M = Au). CO(NH₂)₂ was added to the mixtures and heated for 2 h at 80 °C allowing CO(NH₂)₂ to decompose. The mixtures were cooled, and an excess of NaBH₄ was added dropwise under vigorous stirring. The colors of the mixtures immediately turned from light yellow to red brown and dark red brown for γ -Al₂O₃ and Li₂O/ γ -Al₂O₃ mixtures, respectively indicating the formation of AuNPs. After vigorous stirring for 2 h, the slurries were filtered and washed thoroughly with deionized water until no Cl⁻ was detected in the solutions. The chlorine concentration was followed by titration with AgNO₃. The catalyst was dried overnight at 80 °C, and thoroughly ground to ensure that the particle size was in the order of micrometers.

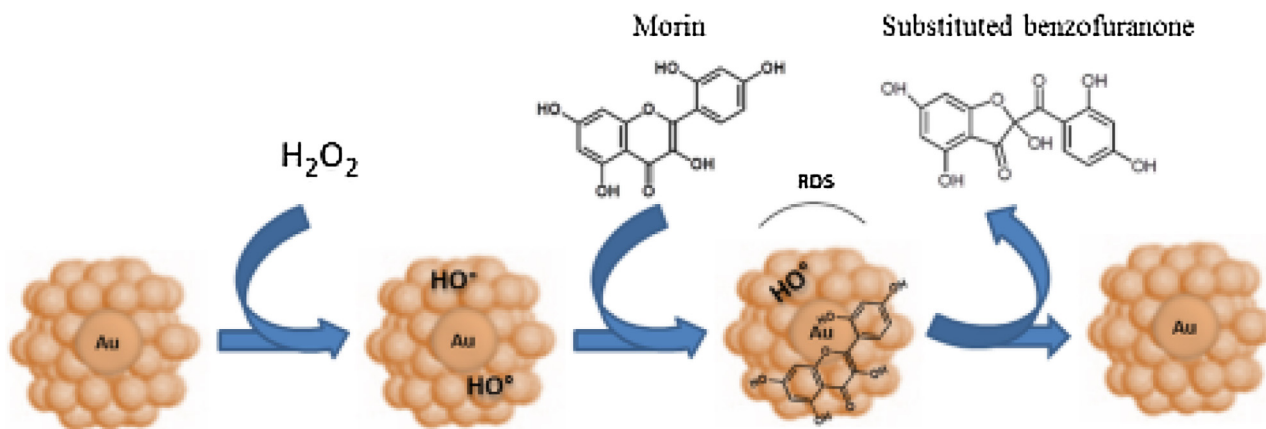


Fig. 2. Langmuir–Hinshelwood mechanism of the oxidation of morin by H_2O_2 in the presence of AuNPs.

2.3. Catalyst characterization

The metal loading was determined by Atomic Absorption Spectroscopy (AAS) using a PerkinElmer AAnalyst 400. For that purpose, a small portion of gold catalysts was dissolved in *aqua regia*. The resulting solution was cooled and transferred to a 50 mL flask, and then diluted to the mark with water. The solution was filtered, and an aliquot of the digested samples was drawn into the instrument. The total surface area, and pore volumes and sizes were determined by the Brunauer–Emmet–Teller (BET) method using a Micromeritics Tristar 3000 surface area and porosity analyzer. The average particle size and the particle size distribution were estimated using Image J software [55] from the micrographs obtained from transmission electron microscopy (HRTEM) using JEOL JEM-2100F electron microscope. X-ray diffraction spectroscopy (XRD) was performed on Phillips Diffractometer Anton Paar TCU 1000 and used to estimate the size of the nanoparticles. The surface areas of gold nanoparticles were determined through ligand adsorption method by ultraviolet–visible spectroscopy (UV–vis) using Shimadzu UV-1800 Spectrophotometer. The thermal behaviour of gold-based catalysts was verified using SDT Q600 thermo gravimetric analyzer (TGA).

2.4. Ligand adsorption

The stock solution of 100 μM 2-MBI was freshly prepared by sonication of the solid salt in deionized water. The reaction was carried out in a 25 mL glass flask at room temperature and atmospheric pressure by suspending 10 mg of the catalysts in 5 mL of various concentrations (5–65 μM) of organothiol solution. After stirring for 17 h, the self-assembly of organothiols molecules on the gold surface was complete. The suspension was immediately centrifuged for 5 min at 10,000 rpm. The centrifuged solution was transferred to an optical cell, and the photometric analysis was performed using UV–vis spectrophotometer. A linear calibration curve for 13 standard solutions of 2-MBI (Fig. S1) was obtained by monitoring the peak intensity at λ 299.7 nm according to Beer–Lambert's law. The % decrease of 2-MBI was calculated using Eq. (1), where A_0 and A_t represent the absorbance at 0 min and 17 h of reaction, respectively.

2.5. Kinetic measurements

The catalytic reaction was carried out in a 50 mL glass flask at room temperature and atmospheric pressure by mixing 10 mL each of dye and peroxide. The reactions were performed in a 0.0125 M carbonate buffer system of sodium bicarbonate and sodium carbon-

ate, which was adjusted with 4 M hydrochloric acid and sodium hydroxide solution to pH 10. The concentrations of reactants in the reactor were 0.05 mM in morin and 0.0125 M in peroxide. After addition of an appropriate amount of catalyst, resulting in an 8.79 mg/L of the gold active phase, the flask was sealed, and allowed to react under continuous stirring. Optical absorbance measurements were taken by pipetting 0.15 mL aliquots of the reaction mixture at various time intervals during the reaction, and quickly diluting with deionized water to 1.5 mL prior to analysis. The diluted solution was immediately filtered to remove any solid particulates which tend to scatter the incident beam, and the filtrate was transferred to an optical quart cell. The absorbance spectrum was measured using a Shimadzu UV-1800 ultraviolet visible light spectrophotometer at a fixed wavelength of λ 410 nm, which is the absorption maximum of morin at pH 10. The absorbance of morin depends on the pH. The pK_a values of morin are 3.5 and 8.1 [56]. The oxidation of morin is increasing with the pH due to the higher deprotonation of morin [49,57]. Furthermore, the pH will influence the decomposition rate of H_2O_2 [58]. A linear calibration curve for morin concentrations was obtained by monitoring the peak intensity at λ 410 nm for a series of standard solutions according to Beer–Lambert's law. The % decrease of morin was calculated using Eq. (1) [59].

$$\% \text{ decrease in morin} = \left(\frac{A_0 - A_t}{A_0} \right) \times 100\% \quad (1)$$

where A_0 and A_t are absorbance at 0 min and at a given time, respectively. The analysis of the kinetic data was performed in terms of the Langmuir–Hinshelwood model [60,61], in which both reactants must be adsorbed on the surface of the nanoparticles. Similar approach has been used in many reactions [54,62,63]. A schematic representation of this model is displayed in Fig. 2; the peroxide reacts on the surface of the nanoparticles leading to adsorbed active species, such as hydroxyl radicals. Concomitantly, morin adsorbs on the surface of the nanoparticles and undergoes a surface reaction with the active species (rate-determining step), and subsequently, the decomposition product of morin desorbs from the surface of the nanoparticles. The rate law for the morin oxidation reaction might be written as Eq. (2).

$$\frac{dc_{\text{morin}}}{dt} = -kc_{\text{morin}}^n c_{\text{H}_2\text{O}_2}^m c_{\text{cat}}^l \quad (2)$$

where c_{morin} , $c_{\text{H}_2\text{O}_2}$ and c_{cat} represent the concentration of morin, H_2O_2 and metal catalyst respectively, and k the rate constant. The catalytic reactions were conducted under *pseudo*-first-order conditions by ensuring a large excess of H_2O_2 , relative to the amount of morin present for the reaction. Therefore, the concentrations of H_2O_2 as well as that of catalyst remained virtually constants

Table 1

AAS metal loading, BET surface area, pore volume and pore size.

Catalyst	Metal loading (wt%)	Surface area (m ² /g)	Pore volume (cm ³ /g)	Pore size (nm)
γ-Al ₂ O ₃	–	174.6	0.27	6.42
Li ₂ O/γ-Al ₂ O ₃	–	147.0	0.21	6.23
Au/γ-Al ₂ O ₃	0.69	173.4	0.27	6.47
Au/Li ₂ O/γ-Al ₂ O ₃	0.50	153.6	0.26	6.76
Au/γ-Al ₂ O ₃ /BF ₄	0.68	167.5	0.26	6.54
Au/Li ₂ O/γ-Al ₂ O ₃ /BF ₄	0.51	162.1	0.26	6.62
Au/γ-Al ₂ O ₃ /PF ₆	0.69	169.3	0.27	6.51
Au/Li ₂ O/γ-Al ₂ O ₃ /PF ₆	0.52	167.1	0.25	6.55

during the course of the reaction. Previous works show that only initial reaction rate was used for the kinetic analysis [54,64]. Hence the apparent rate constant, k_{app} for the oxidation of morin can be defined through Eq. (3).

$$\frac{dc_{morin}}{dt} = -k_1 S c_{morin}^n = -k_{app} c_{morin} \quad (3)$$

where k_1 is the apparent rate constant normalized to the surface area, S of the catalyst. The model assumes that both reactants are adsorbed on the surface of the nanoparticles, and that the rate of morin oxidation, Eq. (4) is dependent on the nanoparticle surface coverage by morin and H₂O₂:

$$\frac{dc_{morin}}{dt} = -k S \theta_{morin} \theta_{H_2O_2} \quad (4)$$

where θ_{morin} and $\theta_{H_2O_2}$ represent the surface coverage values of the nanoparticles by morin and H₂O₂, respectively, and where k the rate constant of the surface reaction. The adsorption of both reactants onto the surface of the nanoparticles was modeled by a Langmuir–Freundlich isotherm, as shown in Eqs. (5) and (6):

$$\theta_{morin} = \frac{(K_{morin} c_{morin})^n}{1 + (K_{morin} c_{morin})^n + (K_{H_2O_2} c_{H_2O_2})^m} \quad (5)$$

$$\theta_{H_2O_2} = \frac{(K_{H_2O_2} c_{H_2O_2})^m}{1 + (K_{morin} c_{morin})^n + (K_{H_2O_2} c_{H_2O_2})^m} \quad (6)$$

where K_{morin} and $K_{H_2O_2}$ refer to the adsorption constants on the catalyst surface for morin and H₂O₂, respectively. The terms n and m are the Freundlich constants, describing the heterogeneity of the catalyst surface for morin and H₂O₂. The Langmuir–Freundlich isotherm takes into account the heterogeneity of the sorbent [61,65]. Therefore, the reaction rate (Eq. (3)) can be rewritten as Eq. (7).

$$-\frac{dc_{morin}}{dt} = \frac{k S (K_{morin} c_{morin})^n (K_{H_2O_2} c_{H_2O_2})^m}{(1 + (K_{morin} c_{morin})^n + (K_{H_2O_2} c_{H_2O_2})^m)^2} = k_{app} c_{morin} \quad (7)$$

Therefore, the rearrangement of Eq. (7) results in Eq. (8), which relates all of the parameters involved in the Langmuir–Hinshelwood model.

$$k_{app} = \frac{k S K_{morin}^n c_{morin}^{n-1} (K_{H_2O_2} c_{H_2O_2})^m}{(1 + (K_{morin} c_{morin})^n + (K_{H_2O_2} c_{H_2O_2})^m)^2} \quad (8)$$

3. Results and discussion

3.1. Catalysts characterization

Prior to the catalytic evaluation of AuNPs the catalysts were characterized. Table 1 summarizes the gold loading, the total surface area, pore volume and pore size. The results show that the actual metal loading was almost equal to the intended metal loadings of 0.70 wt% and 0.54 wt% for γ-Al₂O₃-containing catalysts and Li₂O/γ-Al₂O₃-containing catalysts, respectively. The average metal loading is higher for γ-Al₂O₃ containing catalysts (98.1%) than for

Table 2

TEM average particle size, and 2-MBI particle size and metal surface area.

Catalyst	TEM Particle size (nm)	2-MBI Particle size (nm)	Surface area	
			(m ² /g _{met}) ^a	(m ² /g _{cat}) ^b
Au/γ-Al ₂ O ₃	3.6 ± 0.5	3.6	87.7	0.5
Au/Li ₂ O/γ-Al ₂ O ₃	3.1 ± 0.2	2.9	108.9	0.8
Au/γ-Al ₂ O ₃ /BF ₄	3.2 ± 0.3	3.1	100.8	0.5
Au/Li ₂ O/γ-Al ₂ O ₃ /BF ₄	2.8 ± 0.6	2.4	129.5	0.9
Au/γ-Al ₂ O ₃ /PF ₆	3.5 ± 0.5	3.2	96.3	0.5
Au/Li ₂ O/γ-Al ₂ O ₃ /PF ₆	2.5 ± 0.5	2.2	145.0	1.0

^a Metal surface area per gram of metal.

^b Metal surface area per gram of catalyst.

Li₂O/γ-Al₂O₃ containing catalyst (94.4%). It was observed that the presence of additive, Li₂O has slightly inhibited the gold loading capacity of the catalysts. That can be due to the fact of Li₂O occupying some of the vacancies susceptible to accommodate gold particles in the structure of highly porous γ-Al₂O₃ [19]. The pore volume and pore size for all the catalysts were similar. All the catalysts have shown considerable total surface area, above 150 m²/g. The surface area of the Li₂O/γ-Al₂O₃ support was revealed to be smaller than that of the γ-Al₂O₃ support and all the gold catalysts. The additive probably blocks some of the pores during the first step of the synthesis (pore volume impregnation), resulting in a decrease in the total surface area [19] and, thereafter the pores were unblocked during the following steps.

No significant weight loss of the catalysts confirms the thermal stability of γ-Al₂O₃ supported AuNPs at temperature up to 800 °C. A minor weight loss of up to 6.4% was observed for all the samples (Fig. 3(b)), with a highest weight loss for Au/Li₂O/γ-Al₂O₃/PF₆ catalyst. Fig. 3(a) shows the weight loss of Au/Li₂O/γ-Al₂O₃/PF₆. The curve shows a gradual decrease from 30 °C to 750 °C, and then tends to remain constant. The small weight loss at temperature less than 100 °C is related to the loss of absorbed water in the catalysts, whereas the gradual weight loss observed up to 750 °C can be assigned to the decomposition of the reducing agent chemisorbed onto the catalysts surface.

Representative TEM images and consequent size distribution histograms of gold-based catalysts are shown in Fig. 4. The micrographs obtained for each catalyst were analyzed to determine the average particle diameter and size distribution of the AuNPs. A measurement of at least 350 nanoparticles, assuming virtually spherical and randomly orientated particles was taken for the construction of the size distribution histograms. The AuNPs are homogeneously distributed over the supports. The sizes of the AuNPs for all the catalysts are in the range of 2–6 nm, with the average size of 2.5 ± 0.5 nm for Au/Li₂O/γ-Al₂O₃/PF₆ catalyst. As can be seen in Table 2, the particle sizes of the catalysts with support with additive are slightly smaller than those with support without additive (i.e. 3.1 ± 0.2 nm for Au/Li₂O/γ-Al₂O₃ compared to 3.6 ± 0.5 nm for Au/γ-Al₂O₃). Also of note that the nanodispersity of the AuNPs was much higher for particles synthesized in ILs (i.e. 2.5 ± 0.5 nm for Au/Li₂O/γ-Al₂O₃/PF₆ compared to 3.1 ± 0.2 nm for Au/Li₂O/γ-Al₂O₃ catalyst),

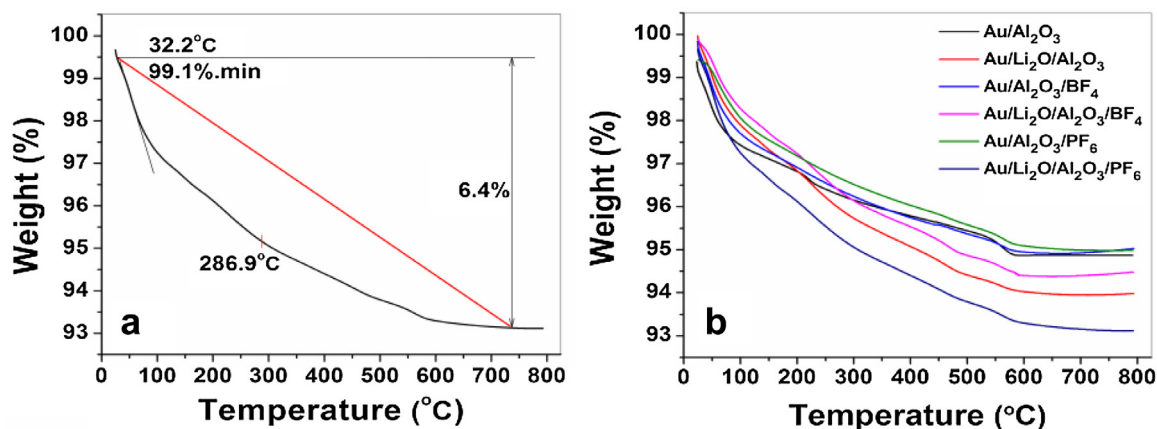


Fig. 3. Thermogravimetric analysis in air from 25 °C to 800 °C of (a) Au/Li₂O/γ-Al₂O₃/PF₆ and (b) different gold-based catalysts.

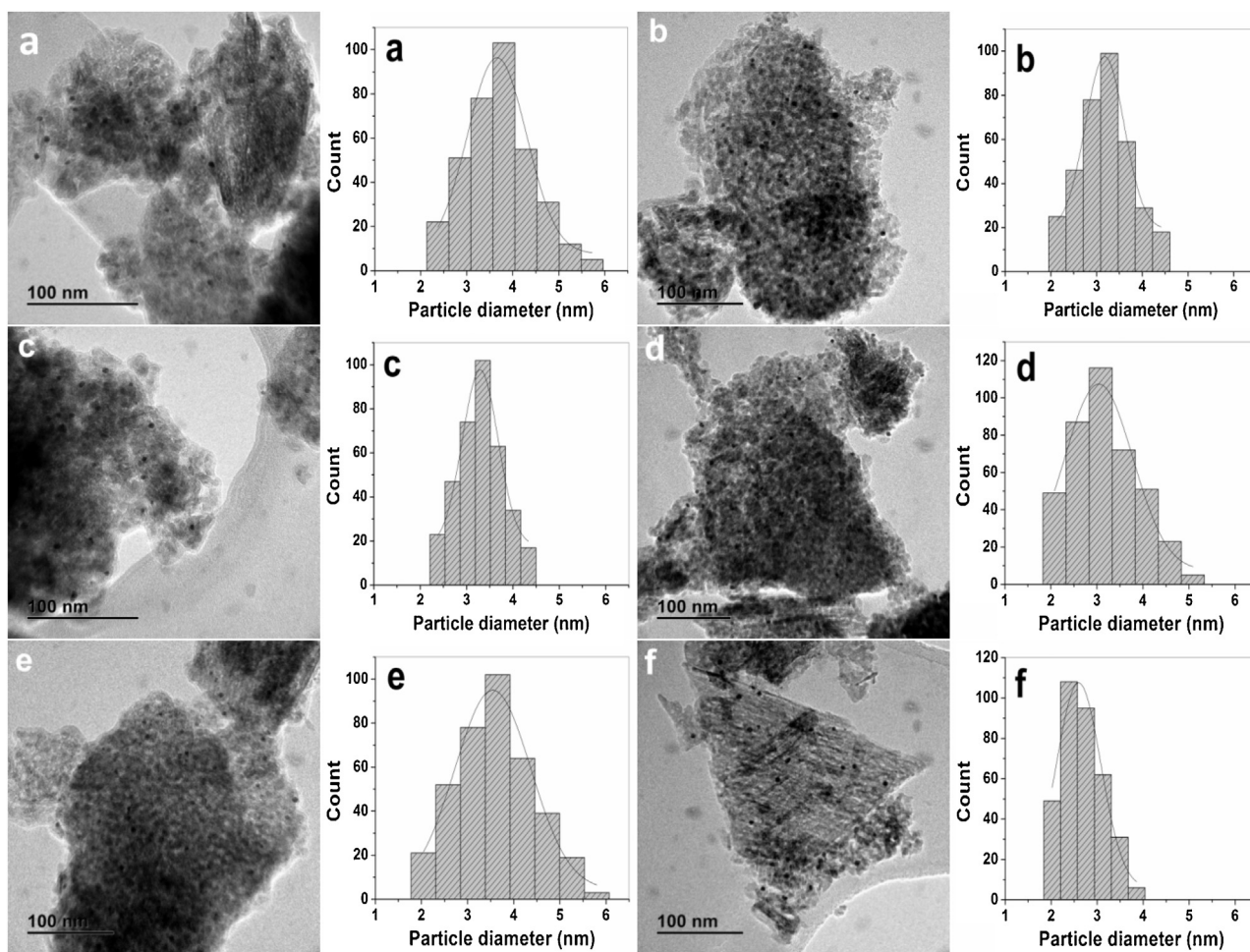


Fig. 4. TEM images and histograms for the size distribution of (a) Au/γ-Al₂O₃, (b) Au/Li₂O/γ-Al₂O₃, (c) Au/γ-Al₂O₃/BF₄, (d) Au/Li₂O/γ-Al₂O₃/BF₄, (e) Au/γ-Al₂O₃/PF₆ and (f) Au/Li₂O/γ-Al₂O₃/PF₆.

as the ILs as well as Li₂O may help slow the nanoparticles grows throughout the preparation of the catalysts [24,26].

3.2. Ligand adsorption

The Langmuir–isotherm was plotted between the unadsorbed amounts of 2-mercaptobenzimidazole, (2-MBI) divided by the adsorbed moles of 2-MBI per gram of gold particle versus the unad-

sorbed amounts of 2-MBI. That Langmuir–isotherm plot was used to determine the effective surface area per gram of the AuNPs [66]. Thus, the reciprocal of the slope of the Langmuir plot was multiplied by Avogadro's number and the cross-section of the probe ligand, 2-MBI molecule (Eq. (9)).

$$A_m = \frac{1}{m} \times N_A \times \sigma \quad (9)$$

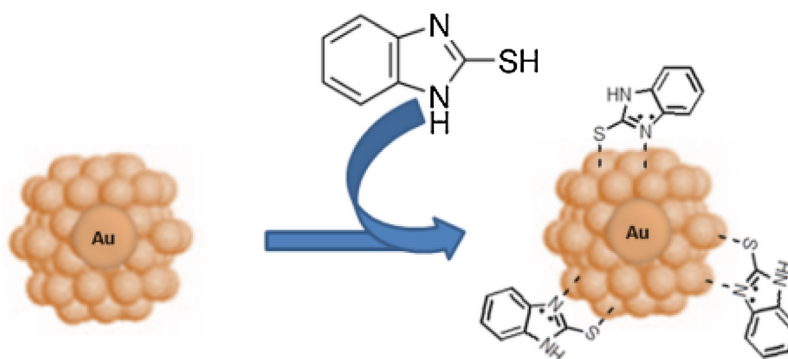


Fig. 5. Schematic description of 2-MBI Chemisorption on the surface of AuNPs (Langmuir–Hinshelwood model).

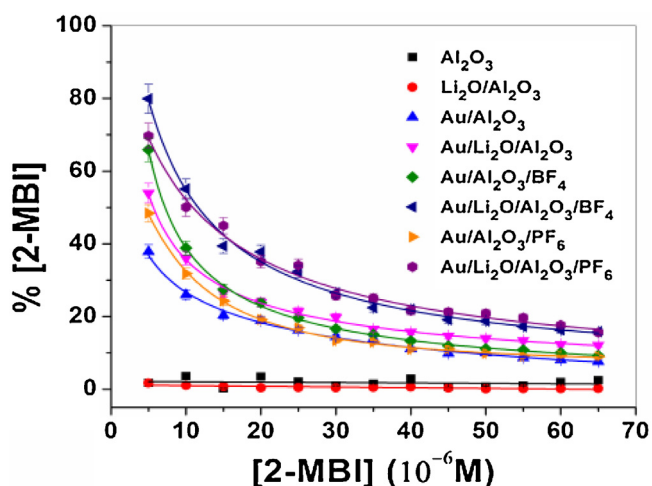


Fig. 6. Percentage adsorption of various concentrations of 2-MBI on supports and their gold-based catalysts after 17 h of reaction.

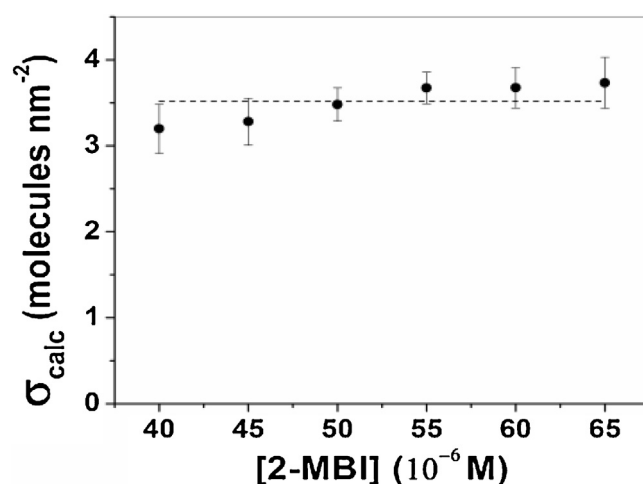


Fig. 7. Calculated packing density as a function of 2-MBI concentration. The dashed lines show the average 2-MBI packing density.

where A_m is the active gold surface area per gram of particle, m is the slope of isotherm plot, N_A is Avogadro's number, and σ is the average surface area which each 2-MBI molecule occupies.

The gold surface area per gram of the sample A_s can be simply determined using Eq. (10). A_m is the area per gram of metal, m_m is the mass of gold in the catalyst sample and m_s is the mass of the catalyst sample.

$$A_s = A_m \times \frac{m_m}{m_s} \quad (10)$$

The average crystallite size, d , that is the diameter of the AuNPs that are assumed faultlessly spherical and mono-dispersed, can be calculated using Eq. (11) [39].

$$d = \frac{F_g}{\rho \times A_m} \quad (11)$$

where F_g is the shape factor (hemisphere = 6), and ρ is the metal density. A study by Ansar et al. showed that 2-MBI on the AuNPs is in the thiolate anion form at neutral pH with a bidentate interaction where both sulfur and the unprotonated nitrogen atom in 2-MBI thiolate interact with AuNPs [45] as shown in Fig. 5.

To assess the contribution of the support on the adsorption of probe molecules on dispersed system, we have first evaluated the adsorption of 2-MBI on the $\gamma\text{-Al}_2\text{O}_3$ and $\text{Li}_2\text{O}/\gamma\text{-Al}_2\text{O}_3$ supports. The adsorption of 2-MBI on the surface of AuNPs was evaluated by using various supported gold catalysts. The ability of the AuNPs to adsorb the probe molecules is expressed as a percent decrease in 2-MBI concentration that occurs after 17 h of reaction. The trend on the degree of adsorption of different concentrations of 2-MBI

on supports and supported gold catalysts (after 17 h of reaction) is shown in Fig. 6. These results show that no adsorption takes place when 2-MBI is exposed to the supports. However, adsorption occurs when supported gold catalysts were used. Therefore, it can be estimated that 2-MBI adsorbs selectively only on AuNPs and not on $\gamma\text{-Al}_2\text{O}_3$ or $\text{Li}_2\text{O}/\gamma\text{-Al}_2\text{O}_3$ supports. This is in agreement with the report in the literature [43]. The percentage adsorption of 2-MBI on the surface of AuNPs decreased with increase in 2-MBI initial concentration. That abatement of the percentage adsorption is more significant for 2-MBI concentrations up to 45 μM , and then tends to remain constant. That dependence can be due to the fact that an increase in 2-MBI concentration leads to a virtually full coverage of the surface of the nanoparticles by 2-MBI molecules. Thus, the surface of the nanoparticles undergoes saturation. It can also be observed that the adsorption of 2-MBI is in general maximal for catalysts with additive and stabilizer.

The average surface area which each 2-MBI molecule occupies, σ was deduced from the packing density of 2-MBI on AuNPs quantified in this study, using the analytical equation established by Elzey et al. [46]. Fig. 7 shows the calculated packing densities, σ_{calc} of 2-MBI on AuNPs. It can be observed that for 2-MBI with concentration greater than 40 μM the calculated packing density of 2-MBI is almost similar. Therefore, for 2-MBI with concentration of 40–65 μM , the calculated packing density of 2-MBI on AuNPs (3.6 nm) is independent on the concentration, ranging from 3.18 to 3.73 nm^{-2} , and averaging $3.53 \pm 0.27 \text{ nm}^{-2}$ which would be equivalent to the saturation capacity of $0.586 \pm 0.04 \text{ nmol cm}^{-2}$. A good agreement was found between the saturation packing density obtained in this study and those reported by Zhang

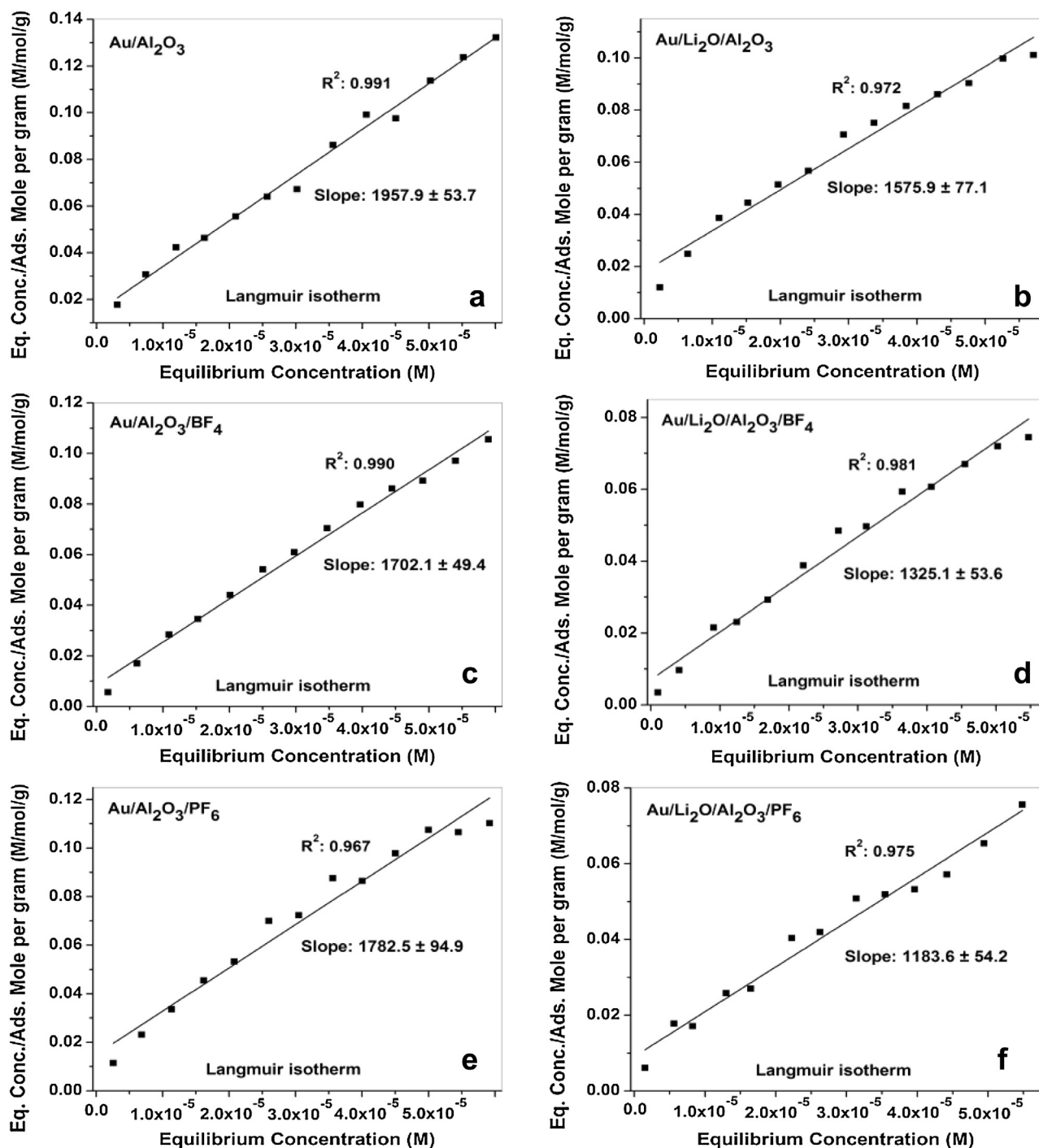


Fig. 8. (a–f) Langmuir isotherm of the adsorption of 2-MBI on supported gold catalysts. The isotherm is constructed by mixing 10 mg of the catalyst with various amount of 2-MBI at $T = 25^\circ\text{C}$ and $t = 17\text{ h}$.

and Ansar [67], $0.571 \pm 0.005\text{ nmol cm}^{-2}$ and Ansar et al. [45], $0.574 \pm 0.006\text{ nmol cm}^{-2}$. On the basis of the packing density, the average surface area which each 2-MBI molecule occupies is $0.285 \pm 0.02\text{ nm}^2$ (calculation shown in Supporting information). This is in agreement with the report in the literature, 0.289 nm^2 [44,45].

The adsorption isotherm of 2-MBI and the Langmuir isotherm for the adsorption of 2-MBI on the surface of the nanoparticles for each supported gold catalyst are shown in Figs. S2 and 8, respectively. The adsorption isotherms showed curved shapes, however

Langmuir isotherms showed straight lines with slopes in the range of 1180–1960.

The surface areas of the AuNPs were revealed to be larger for Li₂O/ γ -Al₂O₃-containing catalysts (average area $127.8 \pm 14.8\text{ g/m}^2$) than for γ -Al₂O₃-containing ones (average area $94.9 \pm 5.4\text{ g/m}^2$). On the other hand, for the catalysts with mixed oxide as support AuNPs stabilized in ILs have revealed larger surface area (average area $137.3 \pm 7.8\text{ g/m}^2$) compared to those synthesized without stabilizer ($108.9 \pm 0.0\text{ g/m}^2$). As mentioned earlier, ILs as well as Li₂O could help slow the AuNPs grows during the preparation of the catalysts, which leads to the higher surface area of the AuNPs. This is in

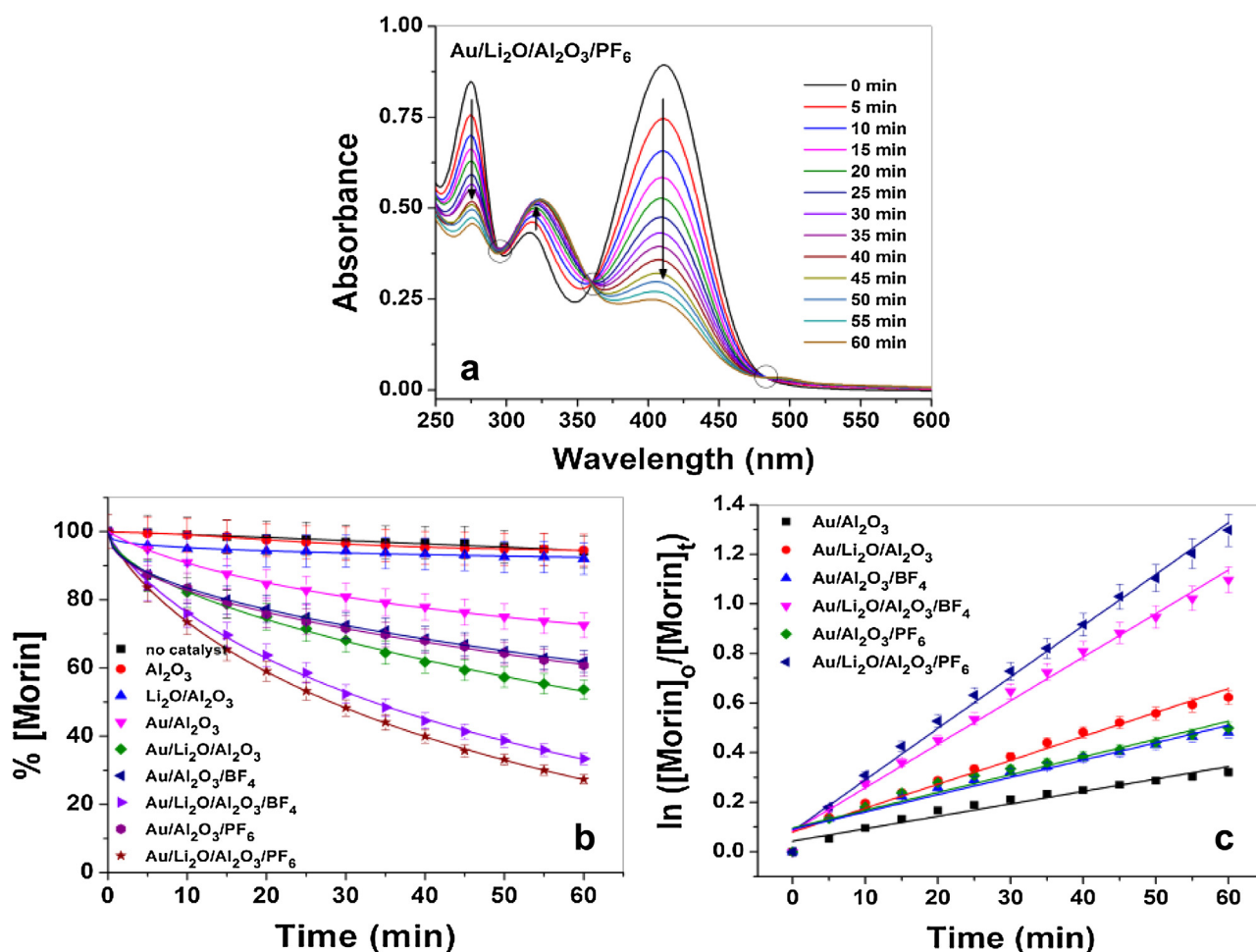


Fig. 9. (a) Change in the UV–vis absorbance spectra of morin using Au/Li₂O/γ-Al₂O₃/PF₆ with H₂O₂. (b) Percentage decomposition of morin with supports and their gold-based catalysts. (c) Kinetic plot of ln[morin] vs time. For all reactions, [morin] = 0.05 mM, [H₂O₂] = 0.0125 M, Catalyst = 8.79 mg/L and T = 25 °C.

agreement with the results obtained with TEM method. The sizes of the AuNPs for all the catalysts are in between 2.2–3.6 nm. The catalyst with larger surface area, Au/Li₂O/γ-Al₂O₃/PF₆ (145.0 m²/g), is characterized by a relatively small particle size, 2.2 nm. Thus, Au/Li₂O/γ-Al₂O₃/PF₆ catalyst is assumed to be more active than the remaining catalysts on the oxidation of morin. It can be observed for both method, TEM and ligand adsorption that the AuNPs synthesized in [BMIM][BF₄] ILs are slightly smaller than that of synthesized in [BMIM][BF₄]. Depending on the preparation method, for the same type of ILs, the sizes of the nanoparticles generated for a specific metal depend on the nature of the counter anions [26]. TEM average gold particle size, and ligand adsorption gold particle size and surface area for fresh catalysts are summarized in Table 2. The average gold particle size could not be determined by XRD because the concentration of gold on the catalyst was below the detection limit of 5% by mass.

Although the specific surface area is the crucial information acquired from the 2-MBI adsorption method, it is worth comparing the obtained particle sizes with those obtained with TEM method. The particle sizes for both TEM (average size 3.1 ± 0.4) and ligand adsorption (average size 2.9 ± 0.5) methods are in general relatively similar. The particle sizes of both methods diverge in the order of 0% for Au/γ-Al₂O₃, 7% for Au/Li₂O/γ-Al₂O₃, 3% for Au/γ-Al₂O₃/BF₄, 15% for Au/Li₂O/γ-Al₂O₃/BF₄, 9% for Au/γ-Al₂O₃/PF₆ and 13% for Au/Li₂O/γ-Al₂O₃/PF₆ catalysts. A fair agreement found between particle sizes obtained from both methods has proven the accuracy of the ligand adsorption method, as developed in this study.

Furthermore, the particle sizes obtained with ligand adsorption method are in general slightly smaller than those determined with TEM. That can be due to the fact that ligand adsorption method can accommodate some morphological irregularity of the AuNPs. In general, for ligand adsorption method, there was observed a trend that an increase in the specific surface area leads to a decrease in the particle size, as would be expected. For all catalysts, the BET surface area is much higher than 2-MBI surface area, as it would be expected. That can be explained by the fact that the BET is not specific to the metal surface, but it gives the total surface area including the large surface area of the supports.

3.3. Activity of gold-based catalysts

The oxidation of morin by H₂O₂ was chosen as the model reaction to evaluate the catalytic activities of the γ-Al₂O₃ supported AuNPs. A systematic comparison of the ability of various catalysts to oxidize morin in the presence of H₂O₂ was made. Without any catalyst and, in the presence of supports alone the degradation of morin with H₂O₂ in the carbonate buffer does not proceed in the time frame of the experiments (Figs. 9(b) and S3). Nevertheless, when alumina supported AuNPs were used, a reaction occurred. This observation shows the crucial catalytic role played by the active species, AuNPs on the oxidation of morin with H₂O₂. The absorption band at λ 410 nm decreases with the progress of the reaction as can be seen in Figs. 9(a) and S4. During the course of the reaction, a new absorbance peak at around λ 321 nm appears which

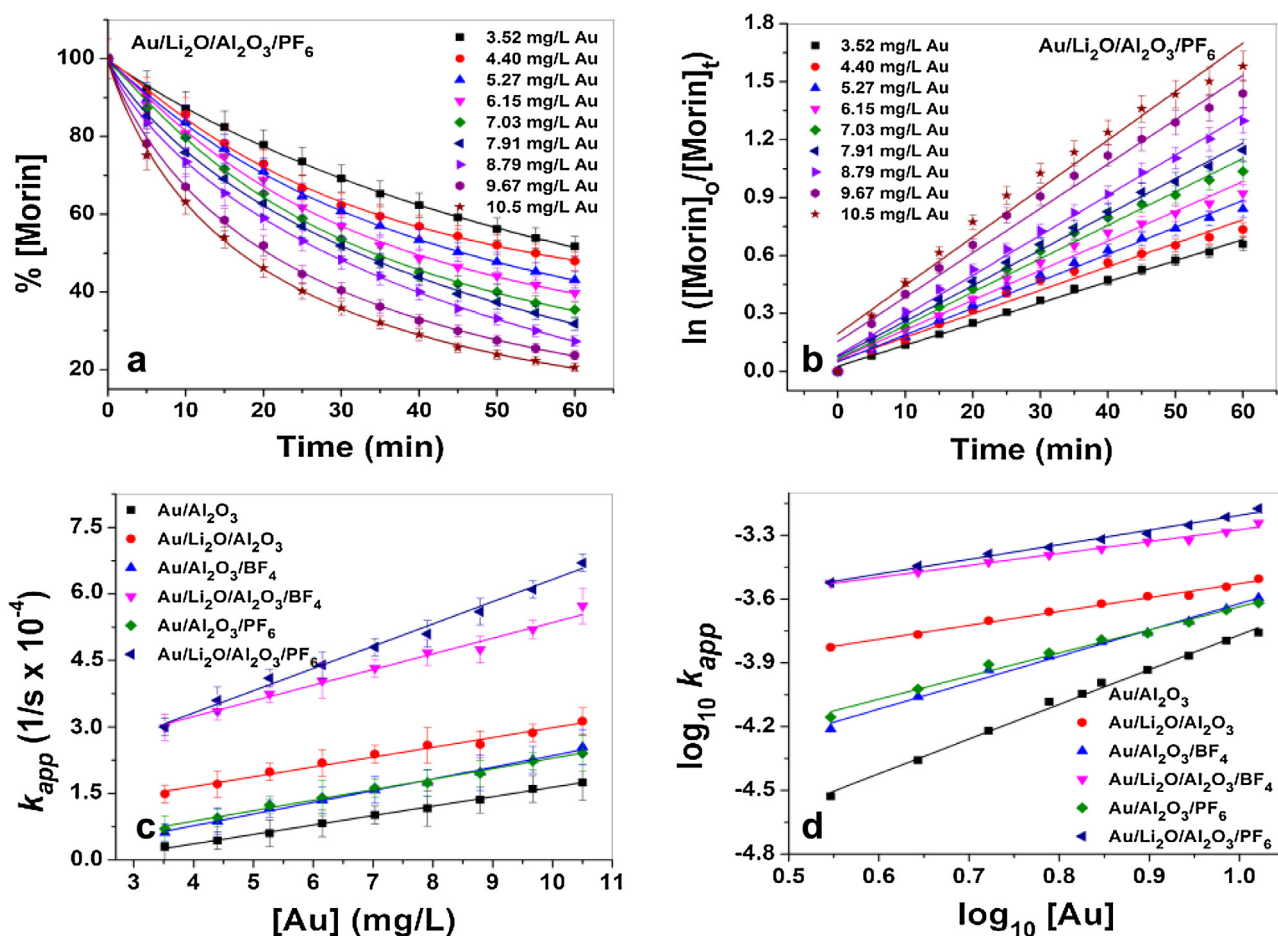


Fig. 10. (a) Percentage decomposition of morin using Au/Li₂O/γ-Al₂O₃/PF₆ with H₂O₂, and (b) kinetic plot of ln([morin]₀/[morin]_t) vs time. (c) Influence of the concentration of Au catalyst on the apparent rate constant k_{app} of the oxidation of morin with H₂O₂, and (d) kinetic plot of log k_{app} vs log [Au] (with slope (a) shown in Table 3). Various concentrations of gold catalysts were reacted with a solution of 0.5 mM morin with 0.0125 M H₂O₂ at 25 °C.

is increasing with time. The isosbestic points at around λ 483, 360 and 294 nm visibly illustrate that morin is oxidizing, and a single intermediate product is formed for the observed time period. This is in agreement with the report in the literature [53,54]. The peak at λ 321 nm has been assigned to a substituted benzofuranone [54,68], an intermediate product that decomposes further to 2,4-dihydroxy benzoic acid and 2,4,6-trihydroxy benzoic acid [51]. However, after a longer reaction time (about 90 min), the isosbestic points start flagging and the peak at λ 321 nm decreases. This phenomenon has been reported by several authors [53,54,68], but with various time of disappearance of the isosbestic points. The disappearance of these isosbestic points has been attributed to a secondary reaction. That is, the decomposition of the intermediate, substituted benzofuranone [43,44,51,68]. In this study, only the initial reaction rate was used for the kinetic analysis. Hence, our kinetic investigation was focused only on the early stage where morin is oxidized to give the initial product.

Each catalysts show different activities with time as can be observed in Fig. 9(b). The activity of the catalysts is expressed as a percent decrease in morin concentration with the progress of the reaction. This quantity is proportional to the color loss of the dye during the reaction. These results show that Li₂O/γ-Al₂O₃-containing catalysts are more active in the oxidation of morin than γ-Al₂O₃-containing catalysts, especially when AuNPs were synthesized in ILs. This is in agreement with the surface area results obtained with thiol method. The surface areas of the AuNPs were revealed to be greater for Li₂O/γ-Al₂O₃-containing catalysts than

for γ-Al₂O₃-containing ones, and the AuNPs stabilized in ILs have shown larger surface area compared to the non-stabilized ones. Thus, high surface area may provide better dispersion of the active sites and easy diffusion of the reactants and, therefore, makes them suitable for catalytic activity. Au/Li₂O/γ-Al₂O₃/PF₆ shows the highest activity (72.7% in 60 min; surface area 145.0 m²/g, particle size 2.2 nm), whereas Au/γ-Al₂O₃ shows the lowest activity (27.5% in 60 min; surface area 87.7 m²/g, particle size 3.6 nm). The positive role of Li₂O on the activity of γ-Al₂O₃ supported AuNPs on the oxidation of morin can be attributed to the effect of Li₂O poisoning the strong acidic sites of the γ-Al₂O₃ support [69]. Based on the obtained results, and the findings by Gluhoi et al. [19,23,24], we believed that the main role of Li₂O on Au/γ-Al₂O₃ catalyst for the oxidation of morin by H₂O₂ is to stabilize the AuNPs i.e. that of a structural promoter. The role of ILs as known [26] was that of the AuNPs stabilizers. AuNPs stabilized by cationic imidazolium ILs provide highly active catalysts for morin oxidation since the coordinating solvent stabilizing the gold surface is weakly bound, preventing AuNPs aggregation without hindering access of the substrates to catalytically active gold sites. In this study, AuNPs stabilized by [BMIM][PF₆] were revealed to be more active than those stabilized by [BMIM][BF₄]. This is in agreement with the AuNPs sizes and surface areas produced from both stabilizers. Fig. 9(c) shows the plot of ln([morin]₀/[morin]_t) versus time of all the catalysts. The linear correlations obtained suggest that the reaction follows pseudo-first-order kinetics with respect to morin oxidation.

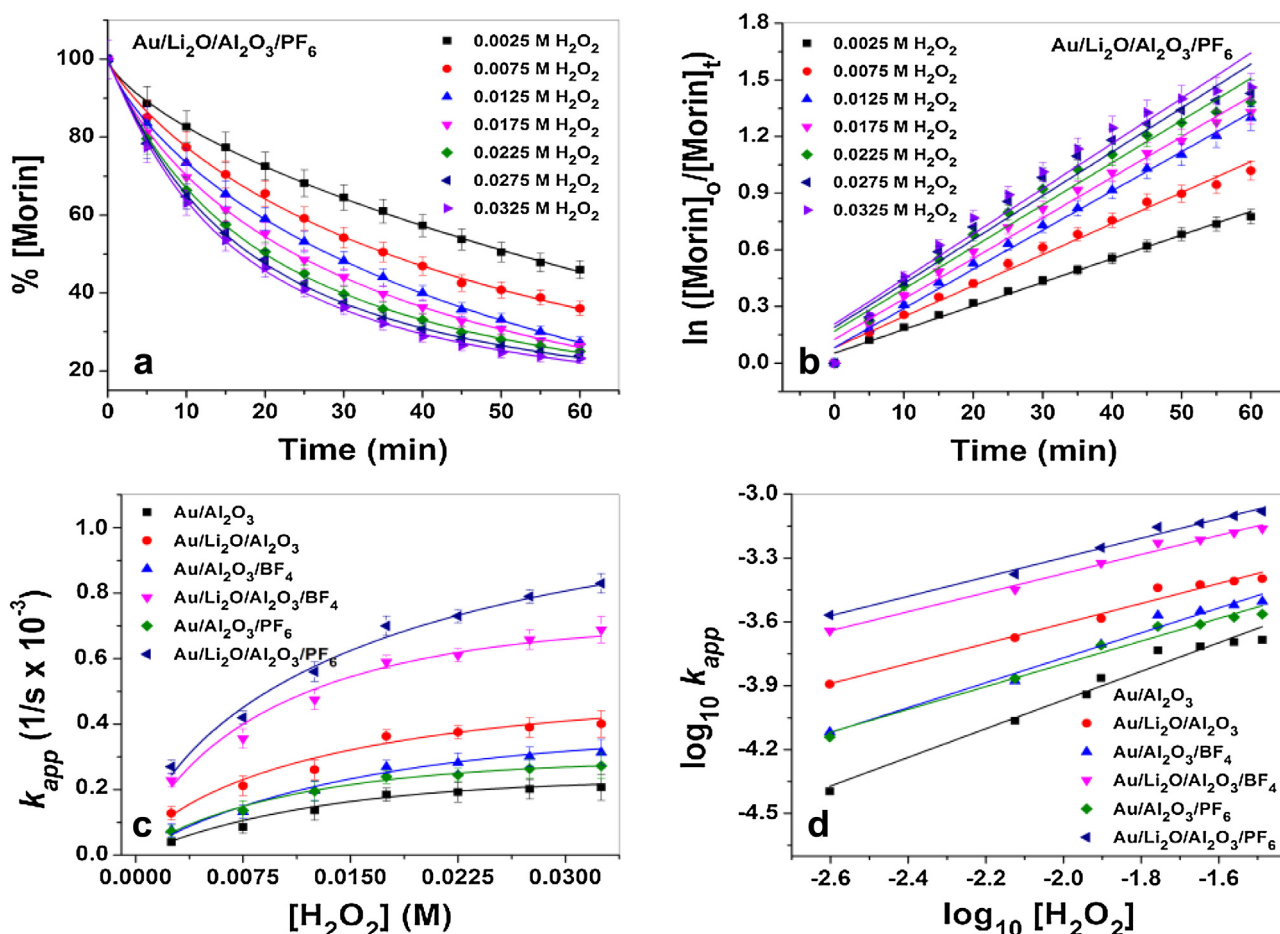


Fig. 11. (a) Percentage decomposition of morin using Au/Li₂O/γ-Al₂O₃/PF₆ with H₂O₂, and (b) kinetic plot of ln[morin] vs time. (c) Influence of the concentration of H₂O₂ on the apparent rate constant k_{app} of the oxidation of morin, and (d) kinetic plot of log k_{app} vs log [H₂O₂] (with slope (b) shown in Table 3). 0.5 mM morin solution was reacted with various concentration of H₂O₂ solution and 8.79 mg/L of Au catalysts at 25 °C.

Since the Au/Li₂O/γ-Al₂O₃/PF₆ catalyst shows the highest activity on the oxidation of morin, further studies were carried out by using mostly that catalyst. It is noteworthy to investigate the role of carbonate buffer (0.0125 M) on the rate of the reaction. In the absence of H₂O₂, the maximum absorption peak of morin did not significantly decrease during the course of the reaction (Fig. S3). It was clear that without H₂O₂ AuNPs did not catalyze the oxidation of morin in carbonate buffer. This suggests that the role of carbonate is mainly for the formation of peroxycarbonate ion radicals, which help to initiate the reaction in the presence of H₂O₂ and active species, AuNPs [53]. Thus, the influence of buffer was not considered during kinetic analysis.

Furthermore, a recycling study of the most active catalyst was performed under the same working conditions. Fig. S5 show that the catalytic activity of the catalyst is almost unaffected (remain high) upon repeated use (70.6% after 1st recycling; 68.9% after 2nd recycling). This is in agreement with the TEM micrographs recorded. TEM image of the catalyst after 2nd recycling shows that the AuNPs remains fairly dispersed, Fig. S6, and the average size measured (2.9 ± 0.4) does not differ significantly from the original size of the fresh catalyst (2.5 ± 0.5). This implies the stability of the AuNPs as synthesized in this study, under the reaction conditions used for this study.

3.3.1. Effect of catalyst concentrations

The rate at which the reaction occurs as a function of catalyst concentration was studied by varying the concentration of the cat-

alyst, whereas keeping those of morin and H₂O₂ constants. It can be seen from Fig. 10(a) that the concentration of morin decreases with increase in catalyst concentration. The apparent reaction rate was plotted against the amount of catalyst present in the system as can be seen in Fig. 10(c). A strictly linear relation is found, showing that the apparent rate constant, k_{app} is proportional to the amount of catalyst present in the system, which could indicate the influence of the surface of the AuNPs in the rate-determining step. Furthermore, the catalytic activity of AuNPs is correlated to the amount of potential active sites based on the total surface atoms. A linear increase in k_{app} with increasing catalyst concentration from 3.5 mg/L to 10.5 mg/L shows that the reaction kinetics measured in this study (catalyst concentration 8.79 mg/L) are not diffusion-controlled. Good linear correlations obtained from Fig. 10(d) show that the oxidation of morin is a first-order reaction with respect to catalyst concentration.

3.3.2. Effect of reagent concentrations

To elucidate the dependence of apparent rate constant, k_{app} in the system, kinetic experiments were performed by keeping the concentration of both catalyst and morin constant while varying that of H₂O₂ as can be seen in Fig. 11. On the other hand, the concentration of morin was varied, while those of catalyst and peroxide were kept constant (Fig. 12). These results revealed that the abatement of morin increased with increase in H₂O₂ concentration as can be observed in part (a) of Fig. 11. However, as the initial morin concentration is increased, there is a decrease in morin decomposition

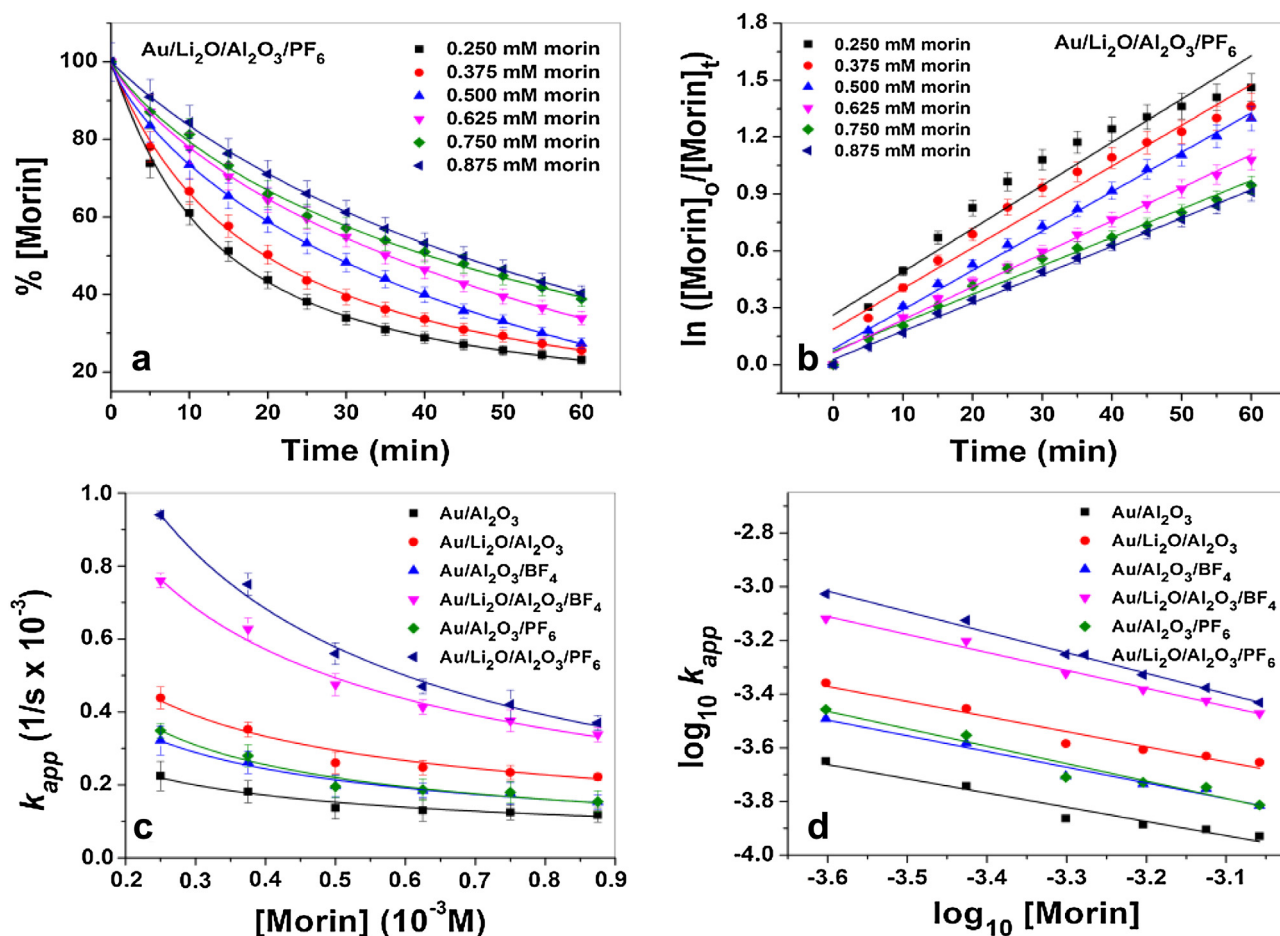


Fig. 12. (a) Percentage decomposition of morin dye solutions using Au/Li₂O/γ-Al₂O₃/PF₆ with H₂O₂, and (b) kinetic plot of ln[morin] vs time. (c) Influence of the concentration of morin on the apparent rate constant, k_{app} with H₂O₂, and (d) kinetic plot of log k_{app} vs log [morin] (with slope (c) shown in Table 3). Various concentrations of morin solution were reacted with 0.0125 M H₂O₂ solution and 8.79 mg/L of Au catalysts at 25 °C.

(Fig. 12(a)). The k_{app} was plotted as a function of the concentration of both H₂O₂ and morin, as can be seen in Fig. 11(c) and Fig. 12(c), respectively. An increase in H₂O₂ concentration leads to an increase in k_{app} , and on the other hand, an increase in morin concentration leads to a decrease in k_{app} as reported for the oxidation of methylene blue by H₂O₂ [62]. The latter behavior was also reported for the oxidation of morin by H₂O₂ with the use of Au-DENs [53] and MnO_x@SPB [54] catalysts. These two findings show that this reaction is not diffusion limited for both reactants, as opposite behavior trends would be observed. The nonlinear dependency of k_{app} with H₂O₂ and morin concentrations suggests a competitive adsorption of both reactants on the AuNPs surface. An optimal concentration of both reactants exists where the reaction rate has a maximum. A linear correlation from Fig. 11(d) and Fig. 12(d) can however well exemplify a pseudo-first-order dependence of the reaction.

3.3.3. Kinetic parameters

The data obtained for this study was modeled in term of Langmuir–Hinshelwood model. The lines fitting in Fig. 11(c) and Fig. 12(c) are derived by fitting the data to that model, with the respective parameters summarized in Table 3. The parameter values boundary are quite restricted and any small variation lead to marked deviations of the experiment data from the model. The values obtained have quantitatively clarified the behavior of k_{app} with the subsequent changes in H₂O₂ and morin concentrations. For Au/Li₂O/γ-Al₂O₃/PF₆ catalyst, for example, the adsorption constant for morin on gold nanoparticles is 20 times higher than that of H₂O₂,

and the Freundlich constants are in the acceptable range value of ≤ 1 . The dependence of k_{app} on the subsequent change in both morin and H₂O₂ concentrations (Fig. 11(c) and Fig. 12(c), respectively) can be justified by the fact that as morin has a significant higher adsorption constant than H₂O₂, an increase in morin concentration leads to a nearly full coverage of the surface of the nanoparticles by morin molecules. Therefore, the surface reaction (the rate-determining step) is hindered, and thus leads to a significant decrease in the reaction of H₂O₂ with the surface of the nanoparticles. The increase in H₂O₂ concentration caused an increase in the apparent rate constant as there are more adsorbed active species, such as hydroxyl radicals on the surface of the nanoparticles, yet the rate of the absorbed molecules is small.

The quality of the obtained kinetic data was validated in more details by plotting $k_{app}[\text{morin}]$ versus $\theta_{\text{morin}}\theta_{\text{H}_2\text{O}_2}$ according to Eq. (12b). This was derived by substituting Eqs. (5) and (6) into Eq. (7) to give Eq. (12a) and afterward rearranged to Eq. (12b).

$$k_{app}c_{\text{morin}} = kS\theta_{\text{morin}}\theta_{\text{H}_2\text{O}_2} \quad (12a)$$

$$kS = \frac{k_{app}c_{\text{morin}}}{\theta_{\text{morin}}\theta_{\text{H}_2\text{O}_2}} \quad (12b)$$

The plots of the data obtained by varying the concentration of morin while keeping that of H₂O₂ constant and vice-versa are shown in Fig. 13(a) and (b), respectively. The slope of the straight line is the product of the kinetic constant, k and the surface area, S of the nanoparticles. Taking in consideration the errors associated to the calculation of both θ_{morin} and $\theta_{\text{H}_2\text{O}_2}$, these values are

Table 3

Summary of the rate constant, k , adsorption constants of morin, K_{morin} and peroxide, $K_{\text{H}_2\text{O}_2}$, the Freundlich Constants, n and m , and the order of the reactions, a , b and c in respect of catalyst and reactants, respectively, at 25 °C by fitting the experimental data with Langmuir–Hinshelwood model and using the power rate law.

Catalyst	k (mol/m ² s)	K_{morin} (L/mol)	$K_{\text{H}_2\text{O}_2}$ (L/mol)	n	m	a	b	c
Au/γ-Al ₂ O ₃	(1.13 ± 0.07) 10 ^{−9}	1827 ± 64	117 ± 29	0.90 ± 0.05	0.56 ± 0.03	1.53 ± 0.04	0.67 ± 0.05	−0.53 ± 0.06
Au/Li ₂ O/γ-Al ₂ O ₃	(1.46 ± 0.04) 10 ^{−9}	1083 ± 54	70 ± 14	0.52 ± 0.04	0.60 ± 0.05	0.65 ± 0.02	0.47 ± 0.03	−0.56 ± 0.06
Au/γ-Al ₂ O ₃ /BF ₄	(1.29 ± 0.05) 10 ^{−9}	1494 ± 71	87 ± 17	0.85 ± 0.07	0.46 ± 0.04	1.24 ± 0.04	0.59 ± 0.04	−0.59 ± 0.05
Au/Li ₂ O/γ-Al ₂ O ₃ /BF ₄	(1.57 ± 0.06) 10 ^{−9}	878 ± 59	58 ± 17	0.69 ± 0.06	0.76 ± 0.04	0.56 ± 0.02	0.45 ± 0.02	−0.67 ± 0.03
Au/γ-Al ₂ O ₃ /PF ₆	(1.32 ± 0.04) 10 ^{−9}	1523 ± 89	92 ± 21	0.75 ± 0.04	0.34 ± 0.09	1.09 ± 0.04	0.53 ± 0.04	−0.65 ± 0.07
Au/Li ₂ O/γ-Al ₂ O ₃ /PF ₆	(1.98 ± 0.03) 10 ^{−9}	798 ± 44	41 ± 11	0.70 ± 0.03	0.95 ± 0.06	0.69 ± 0.02	0.45 ± 0.02	−0.76 ± 0.03

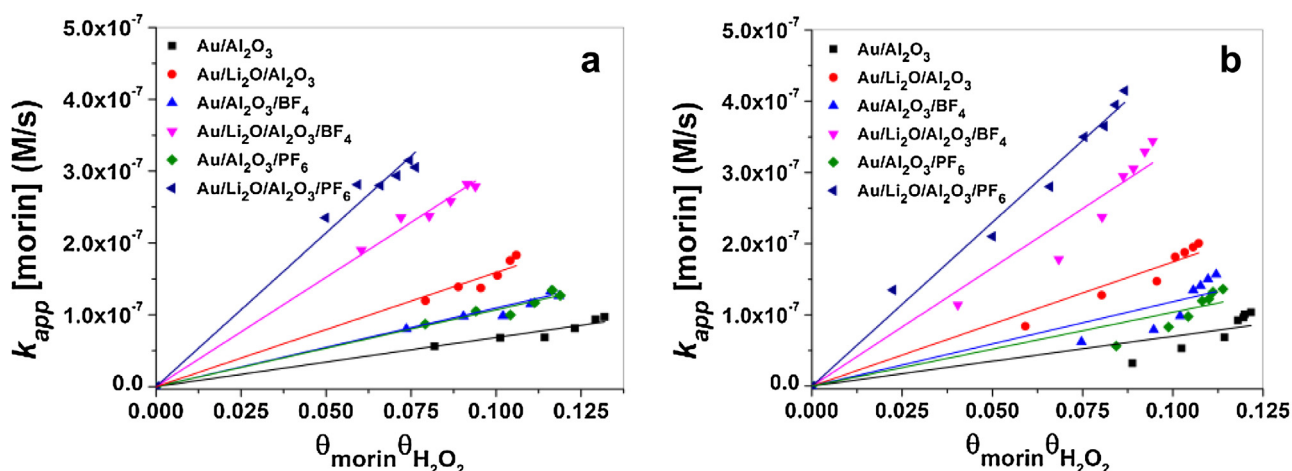


Fig. 13. Kinetic plot of the product of apparent rate constant, k_{app} and morin concentration, $[\text{morin}]$ versus the product of the surface coverage for morin and H_2O_2 , $\theta_{\text{morin}}\theta_{\text{H}_2\text{O}_2}$; (a) for constant H_2O_2 concentration (0.0125 M), and (b) for constant morin concentration (0.0005 M). The solid line is the product of the rate constant k , and surface area S .

in agreement with the calculated values from k and S . For example, for Au/Li₂O/γ-Al₂O₃/PF₆ catalyst with the normalized surface area of 1628 m²/L, the calculated kS value is 3.22×10^{-6} , while the slopes are $(4.29 \pm 0.11) \times 10^{-6}$ and $(4.58 \pm 0.10) \times 10^{-6}$ for constant H_2O_2 concentration and morin concentration, respectively. Thus, the Langmuir–Hinshelwood model is a suitable model for the understanding of this catalytic reaction.

4. Conclusion

This work presents a simple, easy and precise determination of the specific surface area and particle sizes of the AuNPs using 2-mercaptobenzimidazole (2-MBI) as probe ligand. A kinetic study of catalytic activity in morin oxidation of γ-Al₂O₃ supported AuNPs is also presented. The surface areas of the AuNPs were revealed to be larger for catalysts prepared with Li₂O as additive, and for those stabilized in ILs. The correlation between the AuNPs surface area and their catalytic rate was demonstrated where smaller nanoparticles (higher surface area) show a higher catalytic rate. A fair agreement was found between particle sizes obtained from 2-MBI adsorption and TEM methods. All kinetic data were successfully modeled in terms of the Langmuir–Hinshelwood model; that is both reactants are assumed to be adsorbed on the surface of the nanoparticles. The kinetics of the reaction are described in term of the kinetic constant, k describing the surface reactivity of the adsorbed species and the thermodynamic adsorption constants, K of both reactants.

Associated content

Calibration curve of standard solutions of 2-MBI (Fig. S1), Calculation of ligand packing density on AuNPs, Adsorption isotherm of 2-MBI on supported AuNPs (Fig. S2), UV–vis spectra of the oxidation of 2-MBI (Figs. S3 and S4), Percent decrease in morin concentration during the progress of the reaction using fresh and recycled catalyst

(Fig. S5), and TEM image and histogram for the size distribution of recycled catalyst (Fig. S6).

Acknowledgements

This work is based on the research supported in the part by the National Research Foundation of South Africa (Grant specific unique reference number (UID 85386)). We would like also to thank the University of Johannesburg for funding, and Mr. D. Harris and Dr. R. Meyer, Shimadzu South Africa, for the use of their equipment.

Appendix A. Supplementary data

Supplementary data associated with this article can be found, in the online version, at <http://dx.doi.org/10.1016/j.apcatb.2016.06.033>.

References

- [1] N. Dimitratos, J.A. Lopez-Sanchez, G.J. Hutchings, Chem. Sci. 3 (2012) 20–44.
- [2] S. Albonetti, T. Pasini, A. Lolli, M. Blosi, M. Piccinini, N. Dimitratos, J.A. Lopez-Sanchez, D.J. Morgan, A.F. Carley, G.J. Hutchings, F. Cavani, Catal. Today 195 (2012) 120–126.
- [3] M.J. Lippits, B.E. Nieuwenhuys, Catal. Today 154 (2010) 127–132.
- [4] M.J. Lippits, B.E. Nieuwenhuys, J. Catal. 274 (2010) 142–149.
- [5] A.C. Gluhoi, B.E. Nieuwenhuys, Catal. Today 122 (2007) 226–232.
- [6] D. Astruc, Nanoparticles and Catalysis, in: D. Astruc (Ed.), WILEY-VCH Verlag GmbH & Co. KGaA, Weinheim, 2008, pp. 1–48.
- [7] J.D. Aiken, Y. Lin, R.G. Finke, J. Mol. Catal. A: Chem. 114 (1996) 29–51.
- [8] O.A. Belyakova, Y.L. Slovokhotov, Russ. Chem. Bull. 52 (2003) 2299–2327.
- [9] C. Burda, X.B. Chen, R. Narayanan, M.A. El-Sayed, Chem. Rev. 105 (2005) 1025–1102.
- [10] D. Astruc, Inorg. Chem. 46 (2007) 1884–1894.
- [11] D. Astruc, F. Lu, J.R. Aranzas, Angew. Chem. Int. Ed. 44 (2005) 7852–7872.
- [12] A.S.K. Hashmi, G.J. Hutchings, Angew. Chem. Int. Ed. 45 (2006) 7896–7936.
- [13] T.V. Choudhary, D.W. Goodman, Top. Catal. 21 (2002) 25–34.
- [14] R.J.H. Grisel, B.E. Nieuwenhuys, J. Catal. 199 (2001) 48–59.
- [15] G.J. Hutchings, Gold Bull. 29 (1996) 123–130.
- [16] M. Haruta, N. Yamada, T. Kobayashi, S. Iijima, J. Catal. 115 (1989) 301–309.

- [17] M. Haruta, T. Kobayashi, H. Sano, N. Yamada, *Chem. Lett.* 16 (1987) 405–408.
- [18] D. Gavril, A. Georgaka, G. Karaiskakis, *Molecules* 17 (2012) 4878–4895.
- [19] A.C. Gluhoi, N. Bogdanchikova, B.E. Nieuwenhuys, *J. Catal.* 229 (2005) 154–162.
- [20] J. Trawczyński, B. Bielak, W. Miśta, *Appl. Catal. B* 55 (2005) 277–285.
- [21] Y. Rozita, R. Brydson, A.J. Scott, *J. Phys. Conf. Ser.* 241 (2010) 1–4.
- [22] S.A.C. Carabineiro, P.B. Tavares, J.L. Figueiredo, *Appl. Nanosci.* 2 (2012) 35–46.
- [23] A.C. Gluhoi, *Fundamental Studies Focused on Understanding of Gold Catalysis*, Leiden University, Netherlands, 2005, pp. 217.
- [24] A.C. Gluhoi, M.A.P. Dekkers, B.E. Nieuwenhuys, *J. Catal.* 219 (2003) 197–205.
- [25] M.J. Lippits, A.C. Gluhoi, B.E. Nieuwenhuys, *Top. Catal.* 44 (2007) 159–165.
- [26] C. Janiak, *Z. Naturforsch.* 68b (2013) 1059–1089.
- [27] W. Ostwald, *Lehrbuch der Allgemeinen Chemie* 2 (1896) 1.
- [28] G. Schmid, *Nanoparticles: From Theory to Application*, Wiley-VCH ed., Weinheim, Germany, 2010.
- [29] S. Mourdikoudis, L.M. Liz-Marzán, *Chem. Mater.* 25 (2013) 1465–1476.
- [30] Y. Niu, R.M. Crooks, *C. R. Chim.* 6 (2003) 1049–1059.
- [31] Z. Ma, J. Yu, S. Dai, *Adv. Mater.* 22 (2010) 261–285.
- [32] A. Roucoux, J. Schulz, H. Patin, *Chem. Rev.* 102 (2002) 3757–3778.
- [33] J. Krämer, E. Redel, R. Thomann, C. Janiak, *Organometallics* 27 (2008) 1976–1978.
- [34] K. Ueno, H. Tokuda, M. Watanabe, *Phys. Chem. Chem. Phys.* 12 (2010) 1649–1658.
- [35] C. Vollmer, C. Janiak, *Coord. Chem. Rev.* 255 (2011) 2039–2057.
- [36] J. Dupont, J.D. Scholten, *Chem. Soc. Rev.* 39 (2010) 1780–1804.
- [37] M.-A. Neouze, *J. Mater. Chem.* 20 (2010) 9593–9607.
- [38] C.S. Consorti, P.A.Z. Suarez, R.F. de Souza, R.A. Burrow, D.H. Farrar, A.J. Lough, W. Loh, L.H.M. da Silva, J. Dupont, *J. Phys. Chem. B* 109 (2005) 4341–4349.
- [39] A. Janz, A. Köckritz, L. Yao, A. Martin, *Langmuir* 26 (2010) 6783–6789.
- [40] N.V. Vegten, P. Haider, M. Maciejewski, F. Krumeich, A. Baiker, *J. Colloid Interface Sci.* 339 (2009) 310–316.
- [41] M. Clément, H. Ménard, P.A. Rowntree, *Langmuir* 24 (2008) 8045–8049.
- [42] P. Haider, A. Urakawa, E. Schmidt, A. Baiker, *J. Mol. Catal. A: Chem.* 305 (2009) 161–169.
- [43] J.P. Folkers, C.B. Gorman, P.E. Laibinis, S. Buchholz, G.M. Whitesides, R.G. Nuzzo, *Langmuir* 11 (1995) 813–824.
- [44] M. Gadogbe, S.M. Ansar, G. He, W.E. Collier, J. Rodriguez, D. Liu, C.I.-W.D. Zhang, *Anal. Bioanal. Chem.* 405 (2013) 413–422.
- [45] S.M. Ansar, R. Haputhanthri, B. Edmonds, D. Liu, L. Yu, A. Sygula, D. Zhang, *J. Phys. Chem. C* 115 (2011) 653–660.
- [46] S. Elsey, T.D.-H.L. Yu, M. Winchester, V. Hackley, *Anal. Bioanal. Chem.* 403 (2012) 145–149.
- [47] W. Zhang, Z. Yang, X. Wang, Y. Zhang, X. Wen, S. Yang, *Catal. Commun.* 7 (2006) 408–412.
- [48] E.M. Grabowski, E.M. Veldhuizen, A.J.M. Pemen, W.R. Rutgers, *Plasma Sources Sci. Technol.* 16 (2007) 226–232.
- [49] T. Wieprecht, U. Heinz, J. Xia, G. Schlingloff, J.J. Dannacher, *J. Surfactants Deterg.* 7 (2004) 59–66.
- [50] J.J. Dannacher, *J. Mol. Catal. A: Chem.* 251 (2006) 159–176.
- [51] M.P. Colombini, A. Andreotti, C. Baraldi, I. Degano, J.J. Lucejko, *Microchem. J.* 85 (2007) 174–182.
- [52] A. Osman, D.P. Makris, *IFRJ* 18 (2011) 1085–1089.
- [53] M. Nemanashi, R. Meijboom, *Langmuir* 31 (2015) 9041–9053.
- [54] F. Polzer, S. Wunder, Y. Lu, M. Ballauff, *J. Catal.* 289 (2012) 80–87.
- [55] W. Rasband, 2013.
- [56] S.V. Jovanovic, S. Steenken, M. Tasic, B. Marjanovic, M.G. Simic, *J. Am. Chem. Soc.* 116 (1994) 4846–4851.
- [57] T. Wieprecht, M. Hazenkamp, H. Rohwer, G. Schlingloff, J. Xia, *C.R. Chim.* 10 (2007) 326–340.
- [58] N. Kitajima, S. Fukuzumi, Y. Ono, *J. Phys. Chem.* 82 (1978) 1505–1509.
- [59] F.A. Pavan, Y. Gushikem, A.C. Mazzocato, S.L.P. Dias, E.C. Lima, *Dyes Pigm.* 72 (2007) 256–266.
- [60] S. Wunder, Y. Lu, M. Albrecht, M. Ballauff, *ACS Catal.* 1 (2011) 908–916.
- [61] S. Wunder, F. Polzer, Y. Lu, Y. Mei, M. Ballauff, *J. Phys. Chem. C* 114 (2010) 8814–8820.
- [62] M.J. Ndolomingo, R. Meijboom, *Appl. Catal. A: Gen.* 506 (2015) 33–43.
- [63] N.C. Antonels, R. Meijboom, *Langmuir* 39 (2016) 13433–13442.
- [64] Y. Lu, A. Wittemann, M. Ballauff, *Macromol. Rapid Commun.* 30 (2009) 806–815.
- [65] C. Rill, Z.I. Kolar, G. Kinkelbick, H.T. Wolterbeek, J.A. Peters, *Langmuir* 25 (2009) 2294–2301.
- [66] M.A. Mahmoud, B. Garlyyev, M.A. El-Sayed, *J. Phys. Chem. C* 117 (2013) 21886–21893.
- [67] D. Zhang, S.M. Ansar, *Anal. Chem.* 82 (2010) 5910–5914.
- [68] T. Topalovic, *Catalytic Bleaching of Cotton: Molecular and Macroscopic Aspects*, Textile Technology Group, University of Twente, Netherlands, 2007, pp. 183.
- [69] S.R. de Miguel, A.C. Martinez, A.A. Castro, O.A. Scelza, *Chem. Technol. Biotechnol.* 65 (1996) 131–136.